An Integrated Assessment of a G3 GMD Event on Large-Scale Power Grids: From Magnetometer Data To Geomagnetically Induced Current Analysis

Pooria Dehghanian, *Student Member, IEEE*, Anna Zhang, *Student Member, IEEE*, Rida Fatima, *Student Member, IEEE*, Jonathan Snodgrass, *Member, IEEE*, Adam B. Birchfield, *Senior Member, IEEE*, Katherine R. Davis, *Senior Member, IEEE*, and Thomas J. Overbye, *Fellow, IEEE*

***Abstract*—Solar activity can cause geomagnetic disturbances (GMDs) that give rise to geomagnetically induced currents (GICs) which may compromise the reliability of the electric grid. In order to build more reliable models representing GMD interactions with the power grid, the power system's detailed electrical model must be considered along with fluctuations in the earth's magnetic and induced surface electric fields. This study investigates the impact of incorporating spatially varying magnetic fields into surface electric field models on GMD risk metrics. A spatially independent magnetic field model and a spatially varying model are compared through simulations. To perform this analysis, the earth's magnetic field disturbances are transformed into surface electric fields using respective one-dimensional earth conductivity models. Then, the modeling impact of these electric fields is studied using a 2,000-bus grid for Texas and a 25,000-bus grid for the northeast and mid-Atlantic regions of the United States. Simulation results reveal that the inclusion of spatially varying magnetic fields results in considerable differences in GMD risk metrics, highlighting the importance of accounting for spatial variability when assessing GMD risks in the power system.**

***Index Terms*—Geomagnetic disturbance (GMD), magnetometer, geomagnetic field, electric field, geomagnetically induced currents (GICs).**

I. Introduction

This paper aims to elevate understanding of the spatiotemporal properties of geomagnetic disturbances (GMDs) and their impact on the power system through modeling and simulations of spatiotemporally varying electric fields ($\vec{E}$) on large-scale electric grids. Results from power flow analysis are then analyzed to determine risks from GMDs. The work presented in this paper builds on our previous research [1] which conducted statistical analysis to compare magnetic field ($\vec{B}$) data collected from magnetometers installed throughout the United States (US) during a strong (G3) GMD event in early November 2021.

The authors gratefully acknowledge the financial assistance received from the U.S. Department of Energy, Office of Cybersecurity, Energy Security, and Emergency Response (DOE-CESER), and the Pacific Northwest National Laboratory (PNNL) for work conducted under Master Agreement 401273, Task Order 610876.

The authors are with the Department of Electrical and Computer Engineering, Texas A&M University, College Station, TX 77840 USA (e-mail: {pooria.dehghanian; a-zhang; rida.fatima; snodgrass; abirchfield; katedavis; overbye}@tamu.edu)

A. Impact of GMDs on Power Systems

Solar activities such as coronal mass ejections (CMEs) initiate GMDs by ejecting charged particles into space. After traveling to the earth, these particles interact with the earth's conductive ionosphere and can cause a disruption in the earth's magnetic field. When the earth's magnetic field changes, an electric field is induced at the surface of the earth which produces geomagnetically induced currents (GICs) in power transmission systems. Adverse impacts to the power grid's reliability manifest when GICs are high enough to cause degradation of power system equipment such as high-voltage (HV) transformers or cause misoperation of protective relays [2]. Severe impacts of GMDs on the security and operation of the power system, as well as on civilizations that depend on it, were demonstrated by the GMD event of 1989 which resulted in the collapse of the Hydro Quebec power grid, and more recently, the 2003 GMD event which resulted in a cascading blackout of the Swedish grid [3], [4].

Most GMD-related issues arise from GICs flowing through HV transformer windings, causing half-cycle saturation in transformers which results in excessive heating, generation of current harmonics and increased reactive power consumption in transformers [5]. Furthermore, an uncontrolled increase in reactive power load from the transformers can lead to system voltage instability and even power grid collapse if VAR-producing devices such as generators, static var compensators (SVCs), and capacitor banks are unable to produce enough reactive power to meet demand at all system buses, such as what had occurred to the Swedish grid in 2003 [6], [7]. Various strategies have been proposed in the literature to monitor [8], [9], control [10], [11], and mitigate [12], [13] the effects of GICs on the power grid.

B. Efforts to Enhance GMD Modeling

Given the threat GMDs pose to power system security and operation, the power system community in the U.S. has made significant efforts to enhance understanding and improve models of GMDs on the grid. Much of the focus is placed on the integration of physics-based techniques, development of global and regional conductivity models, and data assimilation techniques to improve the precision of geoelectric field models and aid in the mitigation of GMD hazards in the power grid [14]–[16]. For example, several studies have examined and compared differences in electric field estimations when using

1-D and 3-D earth conductivity models [15], [17]–[20]. In this study, the 1-D conductivity model is employed. Considering the primary goal of this work is to understand the importance of incorporating spatially varying geomagnetic fields to estimate induced electric fields, it is deemed acceptable to utilize the 1-D conductivity model in this context.

Another related prior work [19] used sparse magnetometer measurements to model transformer neutral currents and compared their model to measurements collected by the American Transmission Company (ATC) in Wisconsin. Their study demonstrated an important trend: As the distance between the magnetometer and the neutral current measurement location increased, the correlation between modeled and measured currents decreased. These observations reveal important limitations of using a spatially independent magnetic field model for GMD modeling and analysis. Models that oversimplify magnetic field variations across space may lead to inaccuracies in geoelectric field estimations across geomagnetic latitude and for regions with magnetic anomalies, such as those with underground metallic objects or near-space current systems that may impact the geomagnetic field [21]. Inaccurate electric field estimations can impact site assessments for applications such as geophysical surveys, navigation, and GMD analysis.

To address the uncertainty on which non-uniform electric field values to use for GIC modeling, North American Electric Reliability Corporation (NERC) published a benchmark scenario that defines the geoelectric field values employed to calculate GICs [22]. NERC also recommends using scaling factors to account for field changes across geomagnetic latitude and ground conductivity. This study builds on the NERC TPL-007 standard and enhances the current literature by:

- Developing a comprehensive $\vec{B}$-to-$\vec{E}$-to-GIC methodology that takes advantage of magnetic field data collected from spatially distributed magnetometers and corresponding ground conductivity for large-scale power systems.
- Investigating the influence of magnetic field spatial variation on GIC by comparing simulation results using an induced electric field model derived from measurements of spatially distributed magnetometers against a model that was derived from a single reference magnetometer (as in the NERC TPL-007).
- Examining whether NERC's geomagnetic latitude scaling factors properly model spatial variation in the electric field across the grid.
- Demonstrating our results on large-scale synthetic electric grid models including a 2000-bus Texas model and a 25,000-bus northeastern and mid-Atlantic US model.

This study seeks to develop more realistic models for GMD studies by examining the impact of spatial variation in magnetic fields when modeling surface electric fields. A series of steps are considered in this study to perform our investigation:

1) Transformation of time-series magnetometer measurements from six magnetometer stations in Texas and six in the Northeastern (NE) United States into electric fields using corresponding ground conductivity data for separate physiographic regions, as defined in a NERC guideline [2] and Electric Power Research Institute (EPRI) report [23].
2) Statistical analysis of the induced electric fields is performed to glean insights into the relationship between spatio-variations of magnetic field measurements and spatio-variations of the calculated electric fields.
3) Electric fields are used for GIC calculations for two large-scale synthetic grids. The fields are mapped to areas in the grid that correspond to their conductivity zones and closest magnetometer stations.
4) GMD risk assessment: metrics including induced electric field on substations, transformer effective per-phase currents, neutral currents, and the system's reactive power losses are computed using PowerWorld, a power flow simulation software [24].
5) The GIC simulation results are compared to evaluate the impact of spatially varying and spatially uniform magnetic field fluctuations on the power grid. This is achieved by transforming and then modeling electric fields derived from both spatially varying magnetometer measurements and a reference magnetometer waveform.

The rest of the paper is structured as follows. Details on the transformation of the earth's magnetic field into the surface electric field are provided in Section II. Statistical analysis of the time-series electric fields captured and derived from a G3 GMD event is presented in Section III. Scenarios and case studies simulated on the large-scale power grids are shown in Section IV. Results from these studies are discussed in Section V. Finally, Section VI concludes this paper.

II. The Integrated GMD Modeling Method:From B-to-GIC

This section outlines the comprehensive methodology employed in modeling and computing GICs from time-series magnetic field data. A high-level flowchart illustrating the steps involved in GMD modeling and analysis used in this paper can be found in Fig. 1.

A. Magnetic Data Collection

The first step in analyzing geomagnetic disturbances involves determining the resultant fluctuations in the earth's magnetic field using data collected by magnetometers. These instruments are installed at ground level to collect field fluctuations over a period of time, typically with a sampling period ranging from seconds to minutes. Magnetic field data utilized in this study was obtained from two major magnetometer networks: six stations from the Texas A&M University Magnetometer Network (TAMUMN) [25] and six stations from the Distributed Arrays of Small Instruments (DASI) [26]–[28]. These magnetometers capture field fluctuations in TX and the NE regions, respectively. A map of the magnetometers, along with borders drawn to separate different conductivity zones, is displayed in Fig. 2. Magnetic field measurements from these magnetometer networks were then used to derive the earth's surface electric fields.

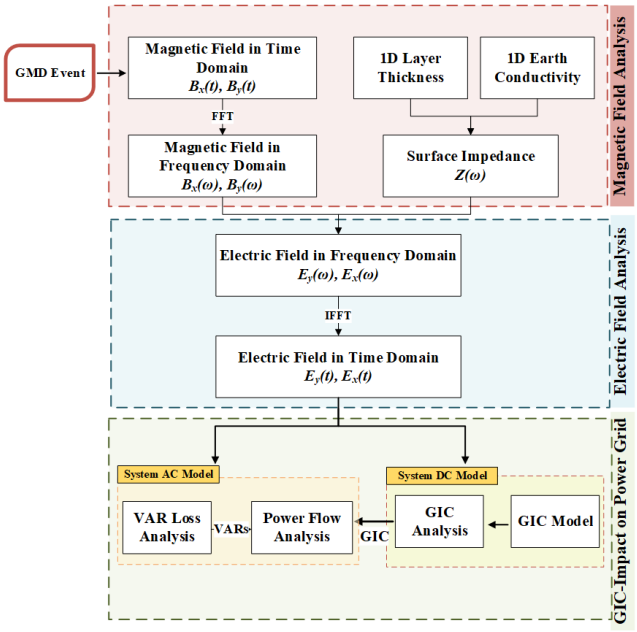

Fig. 1. High-level flowchart of GMD assessments.

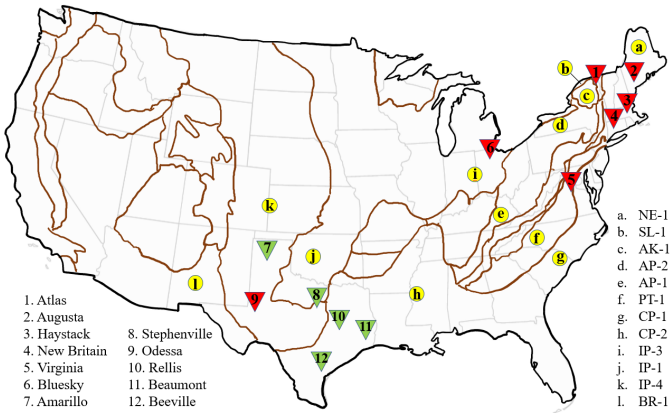

Fig. 2. Locations of magnetometers within the DASI and TAMU magnetometer networks are shown, respectively, in red and green pointers. Borders separating different physiographic regions of the continental United States are also drawn, with all zones containing the 1-D earth conductivity models that were used for this study marked with yellow dots and labeled.

B. Applying Magnetic and Electric Fields onto the Grid

This section provides a concise overview of the process for mapping magnetic fields onto distinct conductivity regions and applying electric fields to the grid. For a more detailed description, the reader may refer to Section IV. A two-step mapping process was applied in the estimation of geoelectric fields across the grid.

1) *Mapping magnetic fields to conductivity regions*: The time-series magnetic fields from each magnetometer station were mapped to the conductivity region that housed the corresponding station. To observe the consequences of neglecting spatially varying magnetic field data in the electric field model, an electric field model was also derived using spatially uniform magnetic fields. This involved mapping the magnetic field collected from one reference magnetometer to all conductivity regions within their respective power grid. Here, it is important to clarify that 'mapping' in this context refers to applying the magnetic field data to the surface impedance model of the region. This process is discussed in detail in Section II-C. The earth resistivity (or conductivity) model for each region was sourced from EPRI and can be downloaded from the EPRI website [29].
2) *Applying electric field estimates to conductivity regions within the grid*: Subsequently, separate time-series electric field estimates corresponding to each station and region were generated. These electric field estimates were then applied to specific conductivity regions within the power grid defined by their GPS coordinates. The auxiliary file containing USGS GPS coordinates for earth conductivity regions was obtained from the PowerWorld website [30].

TABLE I
MAPPINGS BETWEEN CONDUCTIVITY REGIONS AND MAGNETOMETER STATIONS FOR TX

TX-Regions	BR1	IP4	IP1	CP2
Mag. Stations	Odessa	Odessa Amarillo Stephenville	Stephenville	Rellis Beaumont Beeville

TABLE II
MAPPINGS BETWEEN CONDUCTIVITY REGIONS AND MAGNETOMETER STATIONS FOR NE

NE-Regions	**Mag. Stations**	**NE-Regions**	**Mag. Stations**
NE1	Augusta	AP1	Virginia
NE1	Haystack	PT1	Virginia
SL1	Atlas	CP1	Virginia
AK1	Atlas	CP2	Virginia
AP2	New Britain	IP3	Bluesky

For special scenarios in which regions did not have a dedicated magnetometer station, regions were mapped to the nearest station. For instance, the region BR-1 in Texas, which did not have a magnetometer station, was mapped to the nearest station, Odessa. For cases where multiple magnetometer stations shared a single conductivity region, a subdivision strategy was employed. The conductivity region was divided into sub-regions, with each sub-region corresponding to a specific magnetometer station. Each station is then mapped to the sub-region in which the magnetometer station is situated. For example, stations Amarillo, Odessa, and Stephenville all fell within region IP-4 in Texas. To address this, we divided GPS coordinates defining IP-4 into three sub-regions. The area north of 33.00 degrees latitude was mapped to Amarillo while the remaining area east of -99.99 degrees longitude was mapped to Stephenville.

C. Calculating the Electric Fields

In the context of power systems modeling, frequency domain techniques are utilized to approximate the induced surface electric field. This approach involves decomposing the time-series magnetic field measurements, $B(t)$, into its frequency equivalent using the Fast Fourier Transform (FFT).

Given the earth's surface impedance, $Z(\omega)$, magnetic field, $B(\omega)$, and the induced electric field, $E(\omega)$, can be derived.

To approximate $Z(\omega)$, the 1-D layered earth conductivity model published by EPRI [23] is adopted to account for the variation of conductivity within the earth's layers. Although the 1-D model neglects lateral variations in conductivity, it provides a reasonable approximation in most applications. In Tables I and II, the conductivity regions for the grids of TX and NE are displayed with their corresponding magnetometer stations. Some of the stations are represented by multiple conductivity zones. With the depth and conductivity known for each region containing the magnetometer stations, the corresponding impedance observed at the surface of each layer can be obtained. Each layer, n, is characterized by its propagation constant, k_n, which can be calculated using (1), where μ_0 is the magnetic permeability of free space and σ_n is the conductivity of layer n in S/m [2].

$$k_n = \sqrt{j\omega\mu_0\sigma_n} \tag{1}$$

Given k_n, the surface impedance observed at the bottom layer can be obtained by (2).

$$Z_n = \frac{j\omega\mu_0}{k_n} \tag{2}$$

To calculate the surface impedance of the layers above, its reflection coefficient, r_n, must be considered. r_n can be obtained with (3).

$$r_n = \frac{1 - k_n \frac{Z_n + 1}{j\omega\mu_0}}{1 + k_n \frac{Z_n + 1}{j\omega\mu_0}} \tag{3}$$

Using r_n, the impedance seen at the surface of that layer can be obtained by (4), where d_n is the thickness of layer n.

$$Z_n = j\omega\mu_0 \frac{1 - r_n e^{-2k_n d_n}}{k_n(1 + r_n e^{-2k_n d_n})} \tag{4}$$

The steps described by (3) and (4) must be iterated for each layer until the uppermost layer is reached to obtain the final impedance seen at the surface of the earth. Since the propagation constants and respective impedances vary with respect to frequency, the surface impedance calculations described by (1) to (4) must be repeated for each value of ω in order to obtain the final spectral surface impedance, $Z(\omega)$. Given $(Z\omega)$, (5) and (6) can then be used to calculate $E(\omega)$,

$$E_X(\omega) = Z(\omega)\frac{B_Y(\omega)}{\mu_0} \tag{5}$$

$$E_Y(\omega) = -Z(\omega)\frac{B_X(\omega)}{\mu_0} \tag{6}$$

where $E_X(\omega)$ and $E_Y(\omega)$ are the northward and the eastward electric field, respectively. $B_X(\omega)$ represents the northward magnetic field, and $B_Y(\omega)$ corresponds to the eastward magnetic field. The electric field in the time-domain can then be obtained by computing the inverse Fourier transform of $E(\omega)$ as indicated by (7).

$$E(t) = \mathcal{F}^{-1}\{E(\omega)\} \tag{7}$$

D. Modeling GICs in the Power Grid

The surface electric fields can interact with the power grid to induce a quasi-dc voltage V_{dc} across each transmission line. This voltage is computed by integrating E along the incremental length of the transmission line as described below:

$$V_{dc} = \oint E \cdot dl \tag{8}$$

Calculating the GICs which are quasi-dc in nature can be done as follows [31], [32]:

$$\mathbf{I} = \mathbf{G}\,\mathbf{V} \tag{9}$$

where, matrix $\mathbf{G}$ represents the system's conductivity values in conjunction with grounding resistance at the substation. This matrix resembles the bus admittance matrix of a power flow analysis. Voltage vector $\mathbf{V}$ represents the bus voltage and substation voltage. The vector $\mathbf{I}$ are injection currents present at every node in the system, both at the bus and at the substation. A GIC flowing between nodes n and m is calculated by the following equation:

$$I_{nm} = g_{nm}(V_n - V_m) \tag{10}$$

where g_{nm} is the conductance of the transformer or the connecting line in the dc model. For delta-wye transformers, the effective quasi-dc current GIC per phase refers to the current flowing through the high-side winding. It is a combination of the currents flowing through the high and low sides of autotransformers and wye-wye transformers and can be calculated as follows [31]:

$$I^t_{e_f} = |I^t_H + \frac{I^t_L}{\alpha_t}| \tag{11}$$

where, I^t_H and I^t_L denote the per phase effective GIC passing through the high-side and low-side of the transformer coil, respectively, and α_t is the transformer turns ratio parameter. This reactive power loss is a vital link between dc and ac power systems. In the event of a GMD, reactive power loss for transformers in MVAR varies based on the transformer core model, GICs, and voltage and can be linearized as [33]:

$$Q_{Loss} = k.V_{pu}.I_{e_f} \tag{12}$$

where, Q_{loss} is the transformer GIC-related reactive power loss in Mvar, V_{pu} is the per unit voltage and k has units of Mvar/amps. This approach is effective when individual values of k are accessible for each transformer. However, in extensive system studies where default k values are commonly employed, an alternative method is to modify (12) slightly to use an assumed nominal voltage in the definition of k. In this case, the constant value should be adjusted proportionally to the transformer's specific maximum nominal kV level. Consequently, the reactive power loss equation is transformed to: [33]:

$$Q_{Loss} = V_{pu}\,k\left(\frac{V_{Nom\ kV}}{V_{Nom\ kV,Assumed}}\right)I_{e_f} \tag{13}$$

where, $V_{Nom\ kV}$ is the nominal kV of the highest winding for the transformer and $V_{Nom\ kV,Assumed}$ is the assumed nominal voltage. If k is specified for a particular transformer, then the assumed value is just equal to the nominal and (13) is identical to (12).

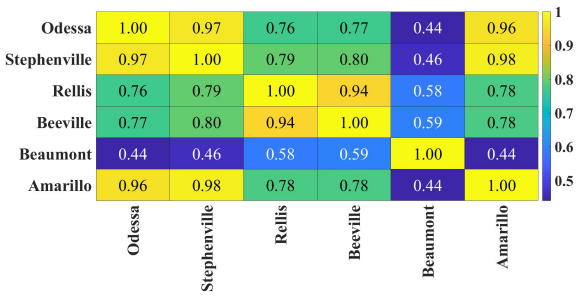

(a) Correlation of the induced $E(t)$ reflected on TX footprint.

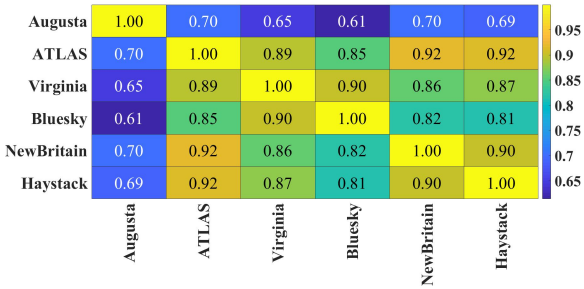

(b) Correlation of the induced $E(t)$ reflected on NE footprint.

Fig. 3. Correlation of the induced $E(t)$ estimations on the peak-storm day (Nov. 4, 2021) for TX and NE.

III. Statistical Analysis of the Induced Electric Fields Across the Stations

This section analyzes the correlation of the estimated induced surface electric fields derived from magnetometer measurements (B_X, B_Y) on the peak-storm day, November 4, 2021. Before beginning the analysis, pre-processing of the magnetic data was performed in order to identify potential outliers. This was accomplished by using the Local Outlier Factor [34], an unsupervised outlier detection technique that evaluates the local density deviation of a point within a given neighborhood. A forward-fill approach was utilized to replace the outliers detected for each station, day, and variable in order to preserve the dimensions of the data and to ensure that comparison for each station at every time point can be made.

Correlation analysis is performed to assess the similarity between time-series electric fields derived from different magnetometer measurements. The strength of the relationship between two data sets is indicated by the magnitude of Pearson's correlation coefficient, which ranges from -1 to 1, where a higher coefficient is indicative of a stronger correlation between data sets. Equation (14) is used to compute the Pearson's correlation coefficients, where $cov(A, B)$ represents the covariance of signals A and B, and σ_A and σ_B are the standard deviations of A and B, respectively.

$$Corr_{A,B} = \frac{cov(A, B)}{\sigma_A \, \sigma_B} \tag{14}$$

In this example, A and B represent the magnitude of the electric fields measured at different locations, where the amplitude of the electric field which is driven by X- and Y- components of magnetic field and can be calculated as follows:

$$|E| = \sqrt{(E_X)^2 + (E_Y)^2} \tag{15}$$

Figure 3 displays the heat map of the correlations between surface geoelectric field magnitudes on the peak-storm day within TX and NE stations. These electric fields were derived from the measured geomagnetic fields and their corresponding ground conductivity. The color bar shows the intensity of the correlations. The heat maps reveal that among all the TX stations, Beaumont and Stephenville exhibit the lowest and highest average correlations in electric field magnitude, respectively, while Atlas and Augusta exhibit the highest and lowest correlations in the NE grid. Notably, Odessa, which exhibited the lowest average magnetic field correlation among TX stations on the peak-storm day [1], does not have the lowest average electric field correlation. From [1], magnetic field correlations within TX were observed to be higher than those within NE. Additionally, the analysis revealed that magnetic field variations did not follow a specific pattern and were generally spatially spread out.

The correlations for the electric fields highlight that patterns for these fields cannot directly be drawn from respective magnetic fields, as induced electric fields are also dependent on the surface impedance of the earth (or, ground conductivity). Therefore, it is essential to account for both the spatially varying magnetic field fluctuations as well as the surface impedance of the respective area in GMD studies. In the following sections, the differences in GMD simulation results from using surface electric field models that were generated from spatially varying and spatially uniform magnetic fields as input are discussed.

IV. Electric Field $E(t)$ Modeling: Scenarios and Case Studies

To assess the modeling effects of GICs in Texas, a synthetic 2,000-bus system was employed to represent the Texas electric grid. Similarly, a synthetic 25,000-bus system was used to represent the northeastern grid. The latter was used to assess the impact of GICs attributed to magnetic field fluctuations measured from the NE region. In the sections following, different combinations of scenarios and case studies will be referenced with their corresponding shortened forms (e.g. TX-C1 refers to studies on the TX grid using electric fields derived from spatially varying magnetic fields, and NE refers to studies on the NE grid), as presented in Table III.

The synthetic electric transmission model developed by Texas A&M University (TAMU) includes intricate models for generators, loads, transmission lines, and other components of the power system. [35], [36] elaborate on the methodology employed to construct these models, highlighting their ability to reliably represent the structural and functional attributes of actual power grids. Once derived, we incorporate the induced surface electric field data sets into these synthetic grids in a three-dimensional format in which the electric field model comprises the latitude and longitude location points as well as temporal data. The following describes the TX and NE grids used in this study, as well as outlines how the case studies were developed.

A. Texas 2,000-bus Synthetic Grid (TX)

This system comprises 2,345 transmission lines, 861 transformers, and 544 generators, which provide a total capacity of 68,727 MW and serve 1,350 load points, amounting to a total demand of 67,109 MW. GMD time-series studies utilizing this grid use an electric field sampling period of 1 s. The bus voltage levels include 24 kV, 115 kV, 161 kV, 230 kV, and 500 kV.

B. Northeastern 25,000-Bus Synthetic Grid (NE)

This system comprises 24,700 transmission lines, 6,030 transformers, and 4,834 generators, which provide a total capacity of 239,694 MW and serve 9,441 load points, amounting to a total demand of 234,527 MW. GMD time-series studies utilizing this grid use an electric field sampling period of 60 s. The bus voltages are comprised of 24 kV, 69 kV, 100 kV, 115 kV, 138 kV, 161 kV, 230 kV, 345 kV, 500 kV, and 765 kV.

Note that the sampling frequency rate is not a critical factor in this study as the focus has primarily been on steady-state GMD analyses. The variation in sampling rates was from the use of two different magnetometer networks: the Texas A&M University Magnetometer Network (applied to the TX grid), which samples every 1 second, and DASI (applied to the NE grid), which samples every minute.

C. Electric Field Model assuming spatially varying $\vec{B}$ (C1)

In case 1, all four conductivity zones contained within the TX and nine in NE are mapped to one or more magnetic field measurements to estimate the induced electric field being modeled. Each conductivity zone as defined by [2] and [23] is bounded by an array of latitude and longitude coordinates within the synthetic grids. In situations where multiple magnetometers share a conductivity zone, such as the IP-4 zone in TX, the location coordinates are sub-divided into areas where each magnetometer is assigned to the area containing its coordinates. The mappings between conductivity zones and magnetometer stations are shown in Tables I for TX and II for NE, respectively. This approach to modeling electric fields considers not only spatial variations caused by different surface impedances as geological structures vary across the earth but also spatial variations exhibited by the magnetic fields due to latitude and longitude effects.

D. Electric Field Model assuming spatially uniform $\vec{B}$ (C2)

In case 2, the effects of magnetic field fluctuations measured by one station per electric grid (the "reference" station) are applied to all conductivity zones within the grid being studied. Although the electric fields estimated by this approach vary across geographical locations due to the effects of ground impedance, this approach of modeling electric fields excludes variations attributed to spatially varying magnetic fields as with the case for the NERC benchmark estimations.

The magnetometer station associated with the lowest average correlation in the electric field as per Fig. 3 was selected as the reference case for each grid. Hence, Augusta and Beaumont magnetometer measurements were selected as the reference for the NE and TX grids, respectively. These stations exhibited the least similarity in induced electric fields when compared to the rest. Using this approach, differences in GICs and other GMD risk metrics between C1 and C2 were accentuated. If a station were chosen randomly without considering the similarity of its electric field to others, the overall conclusions would remain valid, but the observed impact of magnetic field spatial variation on GMD risk metrics would have been less pronounced.

TABLE III
SCENARIOS AND CASE STUDIES BASED ON ELECTRIC FIELD MODELING AND GRID TOPOLOGY

	Scenario 1 (TX)	**Scenario 2 (NE)**
Case 1 (C1)	TX grid assuming spatially varying $\vec{B}$	NE grid assuming spatially varying $\vec{B}$
Case 2 (C2)	TX grid assuming spatially uniform $\vec{B}$	NE grid assuming spatially uniform $\vec{B}$

V. Electric Field $E(t)$ Modeling: Impact Assessment on Large-Scale Grids

In this section, the modeling results for GMD risk metrics, including estimated substation's electric field, transformer effective currents, neutral currents, and reactive power losses are presented using two large-scale synthetic but statistically realistic grids.

A. Electric Field Variations Across Substations

The strength of the earth's induced surface electric field is influenced by various factors, such as fluctuations in the geomagnetic field and earth's ground resistivity. Higher ground conductivity corresponds to a lower ground resistivity (or, impedance) due to the inverse relationship between these two properties. As described by equations (5) to (9), areas of high earth resistivity usually result in stronger electric fields and thus higher GICs. Typically, low substation grounding resistance combined with high earth resistivity results in higher GICs flowing through transmission lines [37]. In addition, the direction of electric fields along transmission lines is shaped by grid configuration, geographical conductivity variations, and line orientation. In addition, the response of nearby substations to GMDs can vary due to differences in grounding systems and soil resistivity, which is influenced by the grid layout. When transmission lines are closely situated, share the same ground conductivity and subject to the same GMD, they experience similar electric fields. Nonetheless, variations in how lines are connected to the grid can result in different GIC characteristics. In some cases, GICs with opposing polarities may be observed in parallel lines. Substations connected to various grid sections or containing parallel lines may experience opposing electric field directions, leading to differing paths for induced currents.

The distribution of electric fields is visualized on the TX and NE grids. Fig. 4a contours the distribution of the electric field for TX-C1 at the time when the peak of 0.1 V/km is reached. The figure illustrates both the strength, as indicated by different color contours, and the direction of the field, indicated by the orientation of the arrows on the map. The sequential color maps described in [38] are used

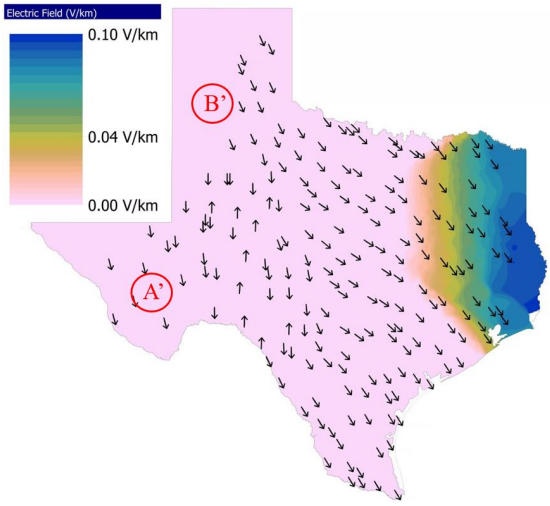

(a) TX-C1 case: Contours of $\vec{E}$ across TX substations at time of peak electric field, calculated using spatially varying $\vec{B}$.

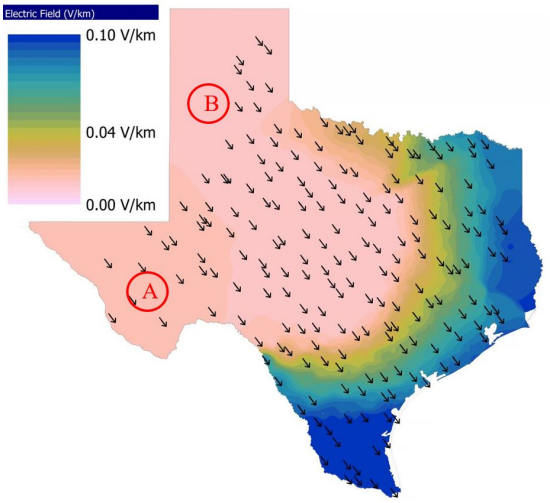

(b) TX-C2 case: Contours of $\vec{E}$ across TX substations at time of peak electric field as measured from the TX-C1 case, calculated using the $\vec{B}$ measured at Beaumont.

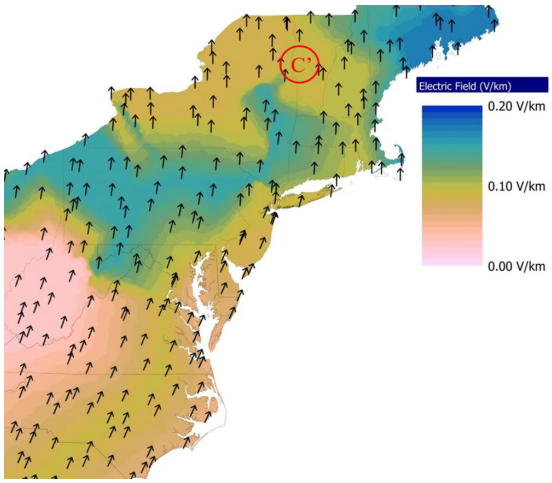

(c) NE-C1 case: Contours of $\vec{E}$ across NE substations at time of peak electric field, calculated using spatially varying $\vec{B}$.

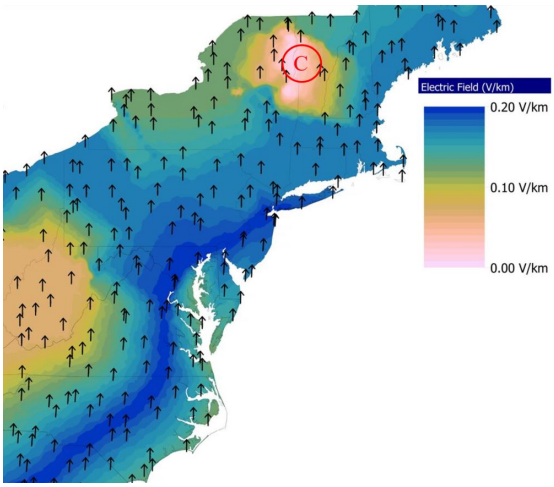

(d) NE-C2 case: Contours of $\vec{E}$ across NE substations at time of peak electric field as measured from the NE-C1 case, calculated using the $\vec{B}$ measured at Augusta.

Fig. 4. Contours of the approximated $\vec{E}$ across substations of the TX and NE synthetic grids at time of peak electric field as measured from the C1 case. Directions of the electric field are indicated by arrows. Specific regions are marked with A, A', B, B', C, and C' for comparison purposes, and are discussed in Section V-A.

for the purpose of better visualizing variations in electric field strength. One can observe that the field peaks at the eastern border of the grid, which is where Beaumont is situated, while the rest of the grid exhibits relatively lower electric fields. This is explained by larger magnetic field fluctuations as measured by the Beaumont magnetometer. Fig. 4b contours the electric field distribution for TX-C2, at the same time-point as C1, for which the magnetic field fluctuations measured in Beaumont are applied on the entire grid. Despite sharing the same range of electric field strength across regions in TX, TX-C2 has peak electric fields that extend along the southeastern region of TX or the CP-2 region where the relative surface impedance is high. Applying scaling factors to electric fields derived from spatially uniform magnetic fields is prescribed by NERC standard TPL-007 to account for geomagnetic latitude effects. The results shown below illustrate that this scaling does not properly model the magnetic field fluctuations caused by varying geography. First, consider equivalent regions A of TX-C2 and A' of TX-C1, as marked in Fig. 4b and Fig. 4a, respectively. These equivalent regions are at roughly the same geomagnetic latitude as Beaumont. Applying a scaling factor of '1' (because latitude did not change) to the electric field at A of TX-C2 to account for latitude effects should produce an electric field magnitude at region A' of TX-C1 to be equivalent to that of region A. However, when the effects of spatial variation in the magnetic field are incorporated as shown in Fig. 4a, the magnitude of the electric field at region A' is 25 times less than that of region A. In addition, areas that are higher in latitude than Beaumont, such as region B' in the TX-C1 case do not experience a larger strength of electric

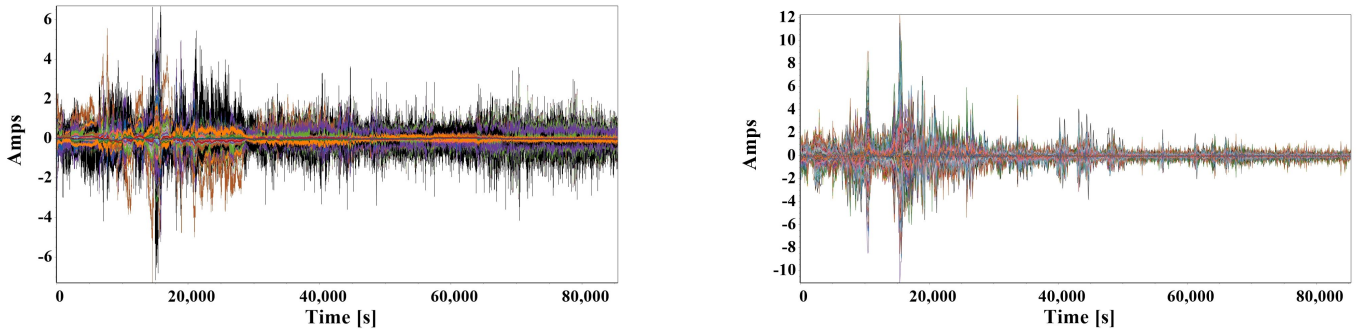

(a) Transformer neutral GICs for TX-C1.

(b) Transformer neutral GICs for NE-C1.

Fig. 5. Transformer neutral GICs for the TX and NE scenarios with the incorporation of the spatial variation of magnetic fields.

field when compared to the same areas, such as area B, in the TX-C2 case. In this situation, the field strength of area B' is 25-times less than that of area B.

The NE grid has also been examined accordingly. Fig. 4c shows a snapshot of the electric field distribution across substations in NE for C1 at the time when the maximum electric field occurs. The field peaks at 0.17 V/km in Augusta and varies across substations and regions. Similar to observations between TX-C1 and TX-C2, the spatial variations of the electric field are considerably different between NE-C1 and NE-C2. Fig. 4d, shows the distribution of electric fields in the NE grid at the same time-point used for C1, assuming spatially uniform magnetic fields as measured from the Augusta station (C2). Notice that the electric field peaks higher than that of NE-C1, at 0.2 V/km with all field orientations in one direction. Despite the range of field strengths being similar between C1 and C2, it is observed that peak intensities of the field occur at different regions between C1 and C2. In C1 when the spatial variation of the magnetic field is considered (Fig. 4c), the field is most intense at NE-1 (Augusta measurements) and AP-2 (New Britain measurements), which are regions of relatively high latitudes. In contrast, when spatial variation is excluded from the model, the electric field intensity peaks at PT-1, which is a region of relatively high surface impedance as shown in Fig. 4d.

As with the TX scenario, it can be inferred that simply applying a scaling factor to the electric field of the NE-C2 case is not sufficient to produce a surface electric field model that adequately captures all local regional variations in the magnetic field. For example, consider the region C of NE-C2 and C' of NE-C1, as marked in Fig. 4d and Fig. 4c: These two regions are the equivalent region across different cases, and is situated at a similar latitude to Augusta. Applying a scaling factor (factor of '1' because the latitudinal distance between Augusta and regions C and C' are approximately zero) to the electric field at region C of NE-C2 to account for latitude effects should yield an electric field magnitude at region C' of NE-C1 to be equivalent to that at region C. However, when regional variations (which also accounts for variations due to latitude) of the magnetic field are incorporated into the induced electric field model as shown in Fig. 4c, region C' exhibits an electric field 7-times that of area C.

These case studies highlight that when the spatial variations of magnetic fields are ignored in electric field models, considerable discrepancies in how electric fields are distributed across the grid can be observed, even when latitude effects have been considered. These discrepancies result in inaccurate modeling of GICs in transformers within the grid and affect the reliability of GMD studies. While these discrepancies may sometimes be small for a mild GMD, but will most likely become much more significant for a more severe GMD.

B. Transformer GICs

Here, the influence of incorporating spatial variations of magnetic fields into electric field models is analyzed with respect to transformer neutral currents, $I_n(t)$. This is accomplished by comparing the magnitude of the neutral currents experienced by all transformers at a time at which the maximum current occurs in C2 for both the TX and NE scenarios. As described by Fig. 6a, the currents for TX are very similar between C1 and C2, with a peak current of 7.2 A and 7.7 A for C1 and C2, at the time of peak current. This was expected because of the high correlation among the TX magnetometers. The time-series for the neutral currents in TX-C1 is displayed in Fig. 5a.

For cases where two distinct transformers exhibit perfect correlation, the explanation is that these transformers experienced the same magnetic field, were located within the same conductivity zone, and thus experienced the same electric field. However, since these transformers have different equivalent impedances (e.g. transformer impedance, line impedance, and substation grounding), which dictates the amount of GIC flow, the amount of GICs through these transformers is different. Although the actual value of their neutral GICs is unequal, they follow the same pattern of change across time.

Figure 6b compares the magnitude of the neutral GICs between C1 and C2 at the time of peak current in C2 within the NE grid. As shown on the figure, there are considerable differences between C1 and C2 with regard to the neutral currents per transformer, with peaks of 9.1 A and 24.4 A, respectively. At this time, the maximum current experienced in NE-C2 is 2.7 times as high as the maximum current observed in NE-C1 when a spatially varying magnetic field is incorporated into the model. The plot also reveals that the neutral currents of identical transformers across C1 and C2 are not as correlated compared to the TX scenario. This is

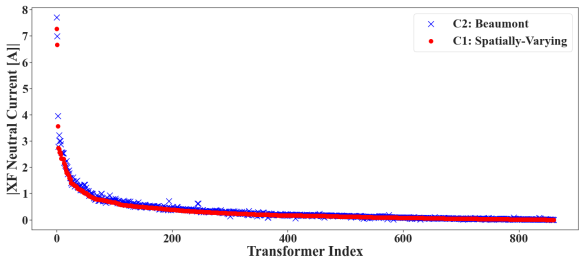

(a) Magnitude of transformer neutral GICs for TX at time of peak GIC as measured from the TX-C2 case. At the time of peak GIC, currents between TX-C1 and TX-C2 are very similar, with a peak current of 7.2 A for the C1 case, and 7.7 A for the C2 case.

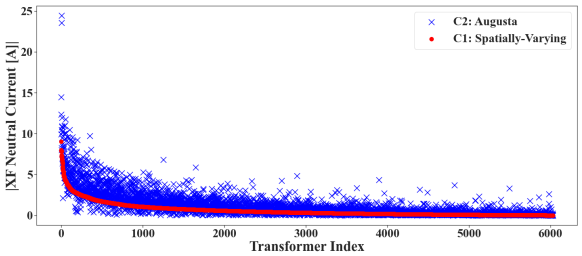

(b) Magnitude of transformer neutral GICs for NE at time of peak GIC as measured from the NE-C2 case. At time of peak GIC, the maximum current experienced in NE-C2 is 2.7 times as high as the maximum current experienced in NE-C1, with a peak current of 9.1 A for the C1 case, and 24.4 A for the C2 case.

Fig. 6. Estimated magnitude of the transformer neutral GICs for the TX and NE scenarios. For both the TX and NE scenarios, all transformers are arranged in decreasing order of $I_n(t)$. Currents shown for the C1 and C2 cases are shown with red dots and blue 'x', respectively.

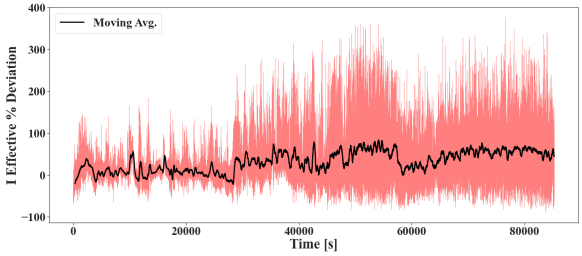

(a) Percent deviation between transformer effective current in TX-C2 with respect to TX-C1, with an average and maximum deviation of 32% and 377%, respectively.

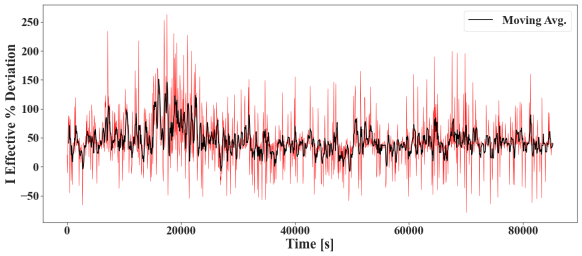

(b) Percent deviation between transformer effective current in NE-C2 with respect to NE-C1, with an average and maximum deviation of 45% and 263%, respectively.

Fig. 7. Percent deviation between transformer effective current for the TX and NE scenarios. The running average with a window size of 5 minutes is used to aid in visualization.

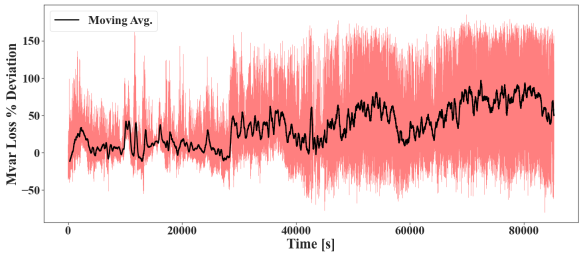

(a) Percent deviation between GIC induced MVAR loss in TX-C2 with respect to TX-C1, with an average and a maximum deviation of 35% and 185%, respectively.

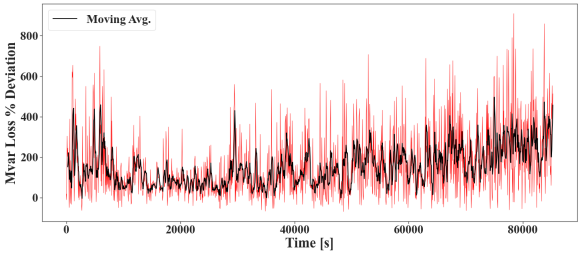

(b) Percent deviation between GIC induced MVAR loss in NE-C2 with respect to NE-C1, with an average and a maximum deviation of 153% and 909%, respectively.

Fig. 8. Percent deviation between GIC induced MVAR loss for the TX and NE scenarios. To better visualize the percent deviation, a running average with a window size of 5 minutes is used for each scenario.

consistent with the relatively low correlation observed between the NE magnetometer measurements. Temporal characteristics of the neutral currents for NE-C1 are shown in Fig. 5b.

Transformer effective currents were also analyzed due to their importance in estimating reactive power losses and transformer heating. The percent deviation of the effective currents over time for C1 and C2 in the TX and NE scenarios are shown in Figs. 7a and 7b, respectively. The running average with a window size of 5 minutes was calculated and used to aid in visualization for each scenario. The maximum deviation for C2 with respect to C1 was 377% and 263% for TX and NE, respectively, with an average deviation of 32% and 45%. While using the absolute value of the deviations can simply the analyses, considering the direction of deviations (positive or negative) provides insight into whether one model type consistently overestimates system impact. The discrepancies presented in these results underscore the importance of incorporating spatial variations in the magnetic field with respect to accurately modeling transformer GICs because neglecting such variations in the model result in less accurate estimations, with some of the results varying significantly.

C. GIC-Induced Reactive Power Loss

Contours of the per-area reactive power losses for each case were created and are shown in Figs. 9a and 9b for TX-C1 and TX-C2, respectively. These maps display the losses

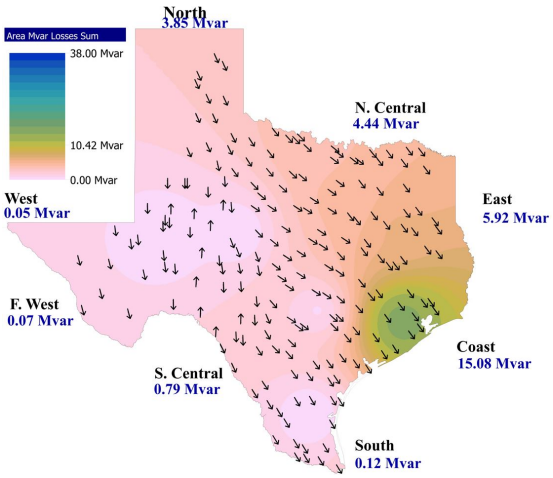

(a) GIC-induced MVAR losses in TX at time of peak electric field, assuming spatially varying $\vec{B}$.

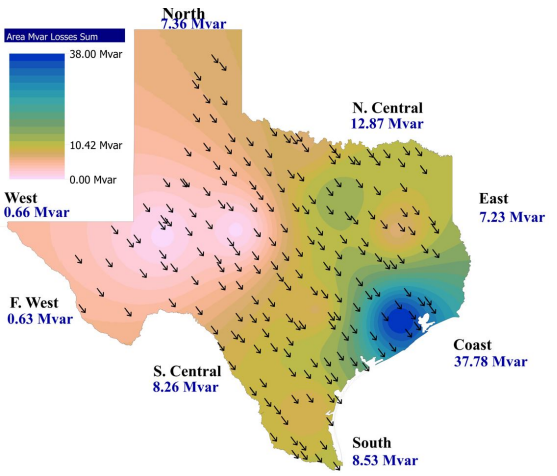

(b) GIC-induced MVAR losses in TX at time of peak electric field as measured from the TX-C1 case. This model was approximated using the $\vec{B}$ measured at Beaumont.

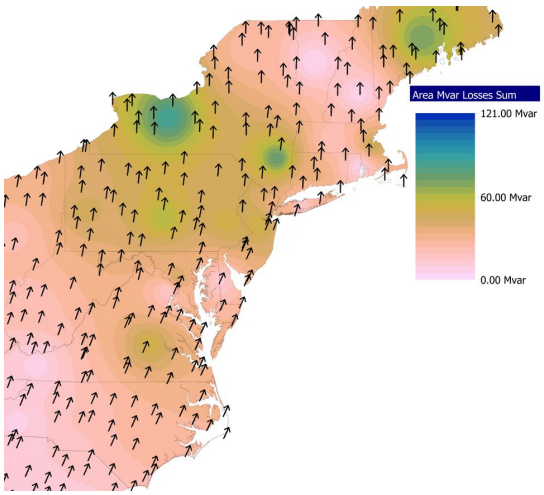

(c) GIC-induced MVAR losses in NE at time of peak electric field, assuming spatially varying $\vec{B}$.

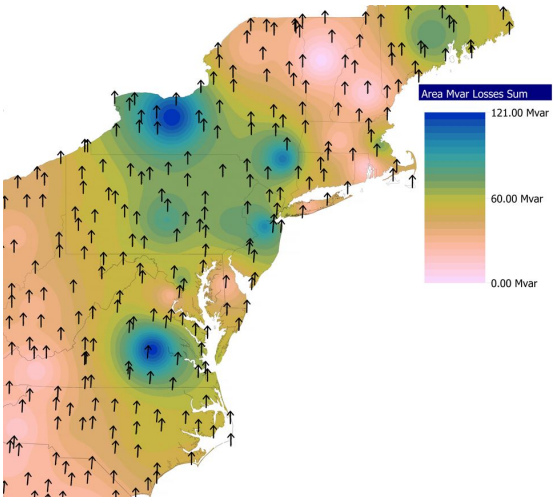

(d) GIC-induced MVAR losses in NE at time of peak electric field as measured from the NE-C1 case. This model was approximated using the $\vec{B}$ measured at Augusta.

Fig. 9. Contour of GIC-induced MVAR losses in the TX and NE footprints. Directions of the electric field are indicated by arrows.

experienced at the time at which C1 experiences its peak electric field. It is worth noting that the peak reactive power loss for TX-C2 was 2.5 times that of TX-C1 at that time. Moreover, the CP-2 (south) region exhibits a reactive power loss of 71 times that of TX-C1, with losses of 8.53 MVAR and 0.12 MVAR for C2 and C1, respectively. This is explained by the fact that Beaumont experienced much higher magnetic field fluctuations relative to those measured by the Beeville magnetometer. A plot of the percent deviation in reactive power losses of C2 with respect to C1 across time is displayed in Fig. 8a, with a maximum deviation of 185% and an average of 35%.

The same analysis for reactive power loss was performed on the NE grid. Contours for reactive power loss at the time at which C1 experiences its peak electric field, are displayed in Figs. 9c and 9d for NE-C1 and NE-C2, respectively. At that time point, the peak reactive power loss observed in C2 was 1.4 times that of C1, with losses of 120 MVAR and 88 MVAR for C2 and C1, respectively. Fig. 8b presents the time-varying percent deviation in reactive power losses of C2 with respect to C1, with a maximum deviation of 909% and an average of 153%.

Due to distinct geomagnetic and earth conductivity characteristics between the TX and NE grids, this analysis compared stations within each grid rather than directly comparing the two grids. Nevertheless, there are notable disparities in the impact of magnetic field modeling on GMD metrics when comparing between these two grids. The Mvar loss shown in Fig. 9 represents just one moment during the peak electric field. The event in its entirety results in a greater reactive power loss, and whether it is significant depends on factors such as the system's topology, voltage levels, existing reactive power compensations, and operational needs. For larger GMD events, the expected Mvar loss would be higher. Nevertheless, the findings described here further emphasize the importance of accounting for regional variations in the magnetic field,

as neglecting these effects results in moderate to significant inaccuracies in the calculated reactive power loss in the power system. The case studies shown in this section demonstrate more severe reactive power losses when effects from these regional differences are neglected.

VI. Conclusions and Discussion

This paper places a particular focus on the influence of spatial variation in magnetic fields on GMD risk metrics by comparing simulation results from two different types of electric field models: one that was transformed from magnetic field fluctuations captured by spatially distributed magnetometers, and the other that only considered field fluctuations from one reference magnetometer.

Simulation results revealed significant discrepancies for GMD risk metrics when models neglect the effects of magnetic field spatial variation, even when latitude effects have been considered. In particular, models neglecting spatial variations yielded impacts that were more severe, as observed through electric field distributions, transformer GICs, and reactive power losses on both TX and NE grids. In the context of power system planning and operation, such differences in the modeled impact could result in taking lines out of service to protect system components even when doing nothing is the best choice. Given that the data used in this analysis was collected during a relatively mild GMD event, it is likely that discrepancies observed in simulations would be much greater for a stronger GMD event.

These findings underscore the importance of incorporating spatial variations into GIC analysis and GMD risk assessment. This analysis helps us better identify vulnerable regions in the power grid during GMD storms and provides valuable insights for implementing strategies to ensure critical infrastructure remains resilient during such events.

Future work would be to improve the geomagnetic latitude scaling factor in the NERC TPL-007 standard so that it may capture more of the effects resulting from regional variations in the magnetic field. While this methodology is valuable in simplifying GMD assessments, the findings from this paper indicate this method does not fully capture all variations in electric field intensity resulting from regional differences in magnetic fields.

References

[1] J. L. Wert, P. Dehghanian, A. Zhang, M. Stevens, R. Guthrie, J. Snodgrass, K. S. Shetye, T. J. Overbye, K. R. Davis, and J. Gannon, "Analysis of magnetometer data from a strong g3 geomagnetic disturbance," in *2022 IEEE Texas Power and Energy Conference (TPEC)*, 2022.

[2] "Application guide: Computing geomagnetically-induced current in the bulk-power system," North American Electric Reliability Corporation (NERC), December 2013.

[3] "Solar storm risk to the north american electric grid," Lloyd's and the Atmospheric and Environmental Research, Inc., Report, 2013.

[4] A. Pulkkinen, S. Lindahl, A. Viljanen, and R. Pirjola, "Geomagnetic storm of 29–31 october 2003: Geomagnetically induced currents and their relation to problems in the swedish high-voltage power transmission system," vol. 3, 2005.

[5] "Geomagnetic disturbances: Their impact on the power grid," *IEEE Power and Energy Magazine*, vol. 11, no. 4, pp. 71–78, 2013.

[6] H. Weng, G. Yang, X. Li, and X. Lin, "The impact of gic on system voltage and generator output," in *Int. Conf. on Electric Utility Deregulation and Restructuring and Power Technologies*, 2015, pp. 1736–1739.

[7] L. R. Bonner and A. Schultz, "Rapid prediction of electric fields associated with geomagnetically induced currents in the presence of three-dimensional ground structure: Projection of remote magnetic observatory data through magnetotelluric impedance tensors," *Space Weather*, vol. 15, pp. 204 – 227, 2017 .

[8] M. Zapella, L. Oliveira, R. Hunt, and D. Stewart, "Solving old problems with new technology: How to monitor and measure gic and opd currents," in *71st Annual Conf. for Protective Relay Engineers (CPRE)*, 2018, pp. 1–8.

[9] Z. M. Lewis, J. Wild, M. Allcock, and M.-T. Walach, "Assessing the impact of weak and moderate geomagnetic storms on uk power station transformers," *Space Weather*, vol. 20, no. 4, p. e2021SW003021, 2022.

[10] C. Basu, M. Padmanaban, S. Guillon, M. de Montigny, and I. Kamwa, "Combining multiple sources of data for situational awareness of geomagnetic disturbances," in *2015 IEEE Power Energy Society General Meeting*, 2015, pp. 1–5.

[11] M. Kazerooni, H. Zhu, K. Shetye, and T. J. Overbye, "Estimation of geoelectric field for validating geomagnetic disturbance modeling," in *IEEE Power and Energy Conference at Illinois (PECI)*, 2013, pp. 218–224.

[12] A. Rezaei-Zare and A. H. Etemadi, "Optimal placement of gic blocking devices considering equipment thermal limits and power system operation constraints," *IEEE Trans. on Power Delivery*, vol. 33, 2018.

[13] C. Klauber and H. Zhu, "Power network topology control for mitigating the effects of geomagnetically induced currents," in *2016 50th Asilomar Conference on Signals, Systems and Computers*, 2016, pp. 313–317.

[14] A. Schultz, G. Egbert, A. Kelbert, T. Peery, V. Clote, B. Fry, and S. Erofeeva, "Staff of the national geoelectromagnetic facility, and their contractors," *USArray TA Magnetotelluric Transfer Functions*, 2006 .

[15] A. Kelbert, "The role of global/regional earth conductivity models in natural geomagnetic hazard mitigation," *Surveys in Geophysics*, vol. 41, no. 1, pp. 115–166, 2020 .

[16] J. J. Love, G. M. Lucas, E. J. Rigler, B. S. Murphy, A. Kelbert, and P. A. Bedrosian, "Mapping a magnetic superstorm: March 1989 geoelectric hazards and impacts on united states power systems," *Space Weather*, vol. 20, no. 5, p. e2021SW003030, 2022 .

[17] R. H.-W. Lee, K. S. Shetye, A. B. Birchfield, and T. J. Overbye, "Using detailed ground modeling to evaluate electric grid impacts of late-time high-altitude electromagnetic pulses (e3 hemp)," *IEEE Transactions on Power Systems*, vol. 34, no. 2, pp. 1549–1557, 2019.

[18] M. Kazerooni, H. Zhu, T. J. Overbye, and D. A. Wojtczak, "Transmission system geomagnetically induced current model validation," *IEEE Transactions on Power Systems*, vol. 32, no. 3, pp. 2183–2192, 2016.

[19] M. D. Butala, M. Kazerooni, J. J. Makela, F. Kamalabadi, J. L. Gannon, H. Zhu, and T. J. Overbye, "Modeling geomagnetically induced currents from magnetometer measurements: Spatial scale assessed with reference measurements," *Space Weather*, vol. 15, no. 10, pp. 1357–1372, 2017.

[20] G. M. Lucas, J. J. Love, and A. Kelbert, "Calculation of voltages in electric power transmission lines during historic geomagnetic storms: An investigation using realistic earth impedances," *Space Weather*, vol. 16, no. 2, pp. 185–195, 2018 .

[21] M. S. Zhdanov, *Foundations of Geophysical Electromagnetic Theory and Methods*. Elsevier, 2017, vol. 43 .

[22] "Benchmark geomagnetic disturbance event description," North American Electric Reliability Corporation (NERC), May 2016.

[23] "One-dimensional earth resistivity models for selected areas of continental United States and Alaska," EPRI, Palo Alto, CA: 2012. 1026430.

[24] PowerWorld. [Online]. Available: https://www.powerworld.com/

[25] K. S. Shetye, R. R. Kumar, C. Klauber, Z. Mao, T. J. Overbye, J. Gannon, and M. Henderson, "Development and electric grid applications of a magnetometer network," *IEEE Open Access Journal of Power and Energy*, vol. 8, pp. 77–84, 2021.

[26] National Science Foundation, "DASI track 2: MagStar- improving the spatial coverage of United States magnetometers for space weather research and operations," 2019, NSF Award Abstract: 1933040.

[27] N. R. Council, "Distributed arrays of small instruments for solar-terrestrial research: Report of a workshop," 2006.

[28] National Science Foundation, "Hazards SEES: Improved prediction of geomagnetic disturbances, geomagnetically induced currents, and their impacts on power distribution systems," 2015, NSF Award Abstract: 1520864.

[29] Electric Power Research Institute, "One-dimensional earth resistivity models for selected areas of continental united states & alaska," https://www.epri.com/research/products/000000000001026430 .

[30] PowerWorld Corporation, "Earth resistivity model for gic calculations," 2022, https://www.powerworld.com/knowledge-base/earth-resistivity-model-for-gic-calculations .

[31] V. D. Albertson, J. G. Kappenman, N. Mohan, and G. Skarbakka, "Load-flow studies in the presence of geomagnetically-induced currents," *IEEE Transactions on Power Apparatus and Systems*, vol. PAS-100, no. 2, pp. 594–607, 1981.
[32] T. R. Hutchins and T. J. Overbye, "The effect of geomagnetic disturbances on the electric grid and appropriate mitigation strategies," in *2011 North American Power Symposium*, 2011, pp. 1–5.
[33] T. Overbye, T. R. Hutchins, K. Shetye, J. Weber, and S. Dahman, "Iintegration of geomagnetic disturbance modeling into the power flow: A methodology for large-scale system studies," in *2012 North American Power Symposium (NAPS)*, 2012 , pp. 1–7.
[34] M. M. Breunig, H.-P. Kriegel, R. T. Ng, and J. Sander, "Lof: Identifying density-based local outliers," *SIGMOD Rec.*, vol. 29, p. 93–104, 2000.
[35] A. B. Birchfield, T. Xu, K. M. Gegner, K. S. Shetye, and T. J. Overbye, "Grid structural characteristics as validation criteria for synthetic networks," *IEEE Transactions on Power Systems*, vol. 32, no. 4, pp. 3258–3265, 2017.
[36] A. B. Birchfield, T. Xu, and T. J. Overbye, "Power flow convergence and reactive power planning in the creation of large synthetic grids," *IEEE Transactions on Power Systems*, vol. 33, pp. 6667–6674, 2018.
[37] A. Kelbert and G. M. Lucas, "Modified GIC estimation using 3-d earth conductivity," *Space Weather*, vol. 18, no. 8, 2020.
[38] F. Crameri, G. E. Shephard, and P. J. Heron, "The misuse of colour in science communication," in *Nature Communications*, vol. 11, 2020.